

BAYESIAN EXPERIMENTAL DESIGN FOR HEAD IMAGING BY ELECTRICAL IMPEDANCE TOMOGRAPHY

N. HYVÖNEN[†], A. JÄÄSKELÄINEN[†], R. MAITY[†], AND A. VAVILOV[†]

Abstract. This work considers the optimization of electrode positions in head imaging by electrical impedance tomography. The study is motivated by maximizing the sensitivity of electrode measurements to conductivity changes when monitoring the condition of a stroke patient, which justifies adopting a linearized version of the complete electrode model as the forward model. The algorithm is based on finding a (locally) A-optimal measurement configuration via gradient descent with respect to the electrode positions. The efficient computation of the needed derivatives of the complete electrode model is one of the focal points. Two algorithms are introduced and numerically tested on a three-layer head model. The first one assumes a region of interest and a Gaussian prior for the conductivity in the brain, and it can be run offline, i.e., prior to taking any measurements. The second algorithm first computes a reconstruction of the conductivity anomaly caused by the stroke with an initial electrode configuration by combining lagged diffusivity iteration with sequential linearizations, which can be interpreted to produce an approximate Gaussian probability density for the conductivity perturbation. It then resorts to the first algorithm to find new, more informative positions for the available electrodes with the constructed density as the prior.

Key words. Electrical impedance tomography, head imaging, Bayesian experimental design, A-optimality, adaptivity, edge-promoting prior, lagged diffusivity

AMS subject classifications. 35Q60, 62K05, 62F15, 65F10, 65N21, 78A46

1. Introduction. This work considers Bayesian *optimal experimental design* (OED) for choosing positions of electrodes for monitoring stroke by *electrical impedance tomography* (EIT). The goal of EIT is to reconstruct (useful information on) the internal conductivity of an imaged physical body from boundary measurements of current and voltage at contact electrodes attached to the boundary of the body. This task constitutes an inverse boundary value problem that is nonlinear and severely illposed. For general information on EIT, we refer to the review articles [6, 14, 48].

We resort to a linearized version of the smoothened *complete electrode model* (CEM) [15, 46, 28] as the forward model for the EIT measurements and aim to choose the positions of the available finite number of electrodes so that they maximize the information on the conductivity changes in a *region of interest* (ROI) that corresponds to an area of the brain affected by a stroke. Our study is motivated by the potential application of EIT to bed-side monitoring of stroke in intensive care [47]: When a stroke patient enters a hospital, a *computed tomography* (CT) image of the patient's head is taken, which reveals the head anatomy and the location of the stroke. In particular, the linearization of the forward model around a background conductivity can be motivated by the goal of detecting regrowth of a hemorrhagic stroke or secondary bleeding induced by an ischemic stroke, both of which are presumed to cause moderate conductivity changes around the initially damaged part of the brain. However, the linearization also considerably simplifies the application of Bayesian OED as explained in the following.

A Bayesian optimal design d^* is defined as an admissible maximizer for the expectation of a given utility function $\Upsilon(w, y; d)$, with the expectation taken with respect to

[†]Aalto University, Department of Mathematics and Systems Analysis, P.O. Box 11100, FI-00076 Aalto, Finland (nuutti.hyvonen@aalto.fi, altti.jaaskelainen@aalto.fi, ruma.maity@aalto.fi, anton.vavilov@aalto.fi). This work was supported the Jane and Aatos Erkko Foundation and the Academy of Finland (decision 348503, 353081).

the data $y \in \mathcal{Y}$ and the parameter of interest $w \in \mathcal{W}$ [1, 12, 42, 44]. In mathematical terms,

$$d^* = \arg \max_{d \in \mathcal{D}} \int_{\mathcal{Y}} \int_{\mathcal{W}} \Upsilon(w, y; d) \pi(w, y | d) dw dy, \quad (1.1)$$

where \mathcal{D} is the space of admissible designs and $\pi(w, y | d)$ is the joint probability density of the parameter and data for the design d . In this work, Υ is chosen to be a *negative quadratic loss function* that measures distance from w to the mean $\hat{w}(y; d)$ of the posterior density $\pi(w | y; d)$, which leads to the concept of Bayesian A-optimality in our linear(ized) setting. Another common choice for Υ is related to the Kullback–Leibler distance between the posterior and prior distributions, which would in turn correspond to Bayesian D-optimality. D-optimality is not considered in this work, although it could be tackled with the same techniques, cf. [30].

For the considered inverse problem of EIT, d determines the positions of the electrodes involved in the design process, w represents the (discretized) change in the conductivity of the imaged head, and y carries the measured potential differences at the electrodes. Due to the employed linearization of the relation between w and y , a Gaussian prior for w and an additive Gaussian noise model that is independent of w enable explicit evaluation of the double integral in (1.1), leading to minimization of a weighted trace of the posterior covariance with respect to d . As mentioned above, this corresponds to finding an A-optimal design [2, 12]. The posterior covariance allows a simple representation in terms of the linearized forward map and the prior and noise covariances, which enables performing the experimental design offline assuming the additive noise process is independent of d . Take note, however, that minimizing the trace of the posterior covariance with respect to d by a gradient-based minimization algorithm requires evaluating derivatives of the linearized forward model with respect to the electrode positions, i.e., computing certain *second* order derivatives of the forward solutions. This setting of experimental design for EIT has been considered in two spatial dimensions in [30] for the standard CEM, but the computation of the required derivatives is computationally more demanding in our three-dimensional setting than in [30].

In addition to the offline optimization of the positions of the electrodes, we also consider an alternative approach that is not as straightforwardly applicable to the bed-side monitoring task used as a motivation above due to the requirement to be able to alter the positions of the electrodes attached to the head of the patient. However, it has potential to not require a CT image of the patient, cf. [10]. The idea is to assume an edge-promoting (weighted and smoothed) *total variation* (TV) prior [43] for the conductivity change in the ROI and to choose an initial set of electrodes for which measurement data is measured (or, in our studies, simulated). A preliminary reconstruction is then formed by combining sequential linearizations and the lagged diffusivity iteration [51]; see [24] for the introduction of this approach to EIT and [10] for its application to head imaging without precise knowledge of the patient’s anatomy. In particular, the initial reconstruction accounts for the nonlinearity of the forward model. According to a Bayesian interpretation [5, 8, 26], the lagged diffusivity iteration also produces a Gaussian approximation for the non-Gaussian posterior induced by the TV prior. The covariance of this approximation can then be employed to find more informative positions for the available electrodes in the same manner as in the offline approach described above, with the aim of using the new positions to better monitor possible further changes in the conductivity close to the initially detected

one, i.e., close to the region initially affected by the stroke. A closely related technique for dealing with a TV prior in Bayesian OED has previously been considered for the linear inverse problems of X-ray and magnetorelaxometry imaging in [25, 26].

Our approach to Bayesian OED is based on linearization and discretization of an inverse boundary value problem for an elliptic partial differential equation. Although convenient in our computationally demanding setting, especially with the TV prior that is not discretization invariant [36], these steps of linearization and discretization are not necessary for formulating and solving Bayesian OED problems for models involving partial differential equations. We refer the reader to [1] for information on the state-of-the-art for such OED problems and note that certain stability properties of Bayesian OED with respect to approximations in the forward model have recently been studied in [20], providing a first step toward formally justifying our approach. In particular, the optimization of electrode positions in EIT has previously been considered in [27, 30, 34, 45]. The papers [30, 34, 45] tackle two-dimensional settings: [30] essentially corresponds to our offline optimization approach in two-dimensions, [45] applies deep learning to the OED problem, and [34] works with the less accurate shunt model [15] and evaluates the expected utility by resorting to a double-loop Monte Carlo method. In [27], a large set of *point electrodes* (cf. [22]) is set at predefined positions, and an optimization method with sparsity constraints for the current injections and potential measurements is applied to select a feasible set of electrodes.

This article is organized as follows. The CEM, its linearization and discretization, as well as the needed derivatives with respect to the electrode positions are introduced in Section 2. Section 3 recalls the basics of finite-dimensional Bayesian inversion, including the Bayesian interpretation of the lagged diffusivity iteration and the reconstruction algorithm based on sequential linearizations used in connection to the TV prior. Section 4 considers OED and introduces the related numerical optimization algorithms. Section 5 documents the numerical experiments, and Section 6 contains the concluding remarks.

2. Complete electrode model. This section recalls the CEM and its derivatives with respect to the conductivity and the electrode contacts and positions. We also introduce the discretized computational models that are used in the numerical experiments.

2.1. Forward problem. Let $M \in \mathbb{N} \setminus \{1\}$ contact electrodes E_1, \dots, E_M be attached to the boundary of the imaged head that is modeled as a bounded Lipschitz domain $\Omega \subset \mathbb{R}^3$. The electrodes are represented as open connected subsets E_1, \dots, E_M of the boundary $\partial\Omega$ with mutually disjoint closures. The union of the electrodes is denoted by $E = \cup E_m$. A single measurement of EIT consists in driving a net current pattern $I \in \mathbb{C}_\diamond^M$ through the electrodes and measuring the resulting constant electrode potentials $U \in \mathbb{C}_\diamond^M$, with

$$\mathbb{C}_\diamond^M = \left\{ V \in \mathbb{C}^M \mid \sum_{m=1}^M V_m = 0 \right\}.$$

The current pattern I belongs to \mathbb{C}_\diamond^M due to conservation of charge and U based on an appropriate choice for the ground level of potential. The latter vector is identified in the following with the piecewise constant function

$$U = \sum_{m=1}^M U_m \chi_m, \tag{2.1}$$

where χ_m is the characteristic function of E_m on $\partial\Omega$.

A mathematical model that accurately predicts real-life EIT measurements is the CEM [15]. Here we employ its smoothed version [28] that carries better regularity properties without severely compromising modeling accuracy. According to the smoothed CEM, the electromagnetic potential u inside Ω and the potentials on the electrodes U satisfy the elliptic boundary value

$$\begin{aligned} \nabla \cdot (\sigma \nabla u) &= 0 && \text{in } \Omega, \\ \nu \cdot \sigma \nabla u &= \zeta(U - u) && \text{on } \partial\Omega, \\ \int_{E_m} \nu \cdot \sigma \nabla u \, dS &= I_m, && m = 1, \dots, M, \end{aligned} \quad (2.2)$$

interpreted in the weak sense and with ν denoting the exterior unit normal on $\partial\Omega$. The conductivity σ is assumed to be isotropic and belong to

$$L_+^\infty(\Omega) := \{\varsigma \in L^\infty(\Omega) \mid \text{ess inf Re}(\varsigma) > 0\}, \quad (2.3)$$

whereas the contact conductivity ζ is modeled as an element of

$$\mathcal{Z} := \{\xi \in L^\infty(E) \mid \text{Re } \xi \geq 0 \text{ and } \text{ess sup}(\text{Re}(\xi|_{E_m})) > 0 \text{ for all } m = 1, \dots, M\}, \quad (2.4)$$

which is interpreted as a subset of $L^\infty(\partial\Omega)$ via zero-continuation. The variational formulation of (2.2) is to find $(u, U) \in \mathcal{H}^1 := H^1(\Omega) \oplus \mathbb{C}_\diamond^M$ such that

$$B_{\sigma, \zeta}((u, U), (v, V)) = I \cdot V \quad \text{for all } (v, V) \in \mathcal{H}^1, \quad (2.5)$$

where \cdot denotes the real dot product and the bounded and coercive bilinear form $B_{\sigma, \zeta} : \mathcal{H}^1 \times \mathcal{H}^1 \rightarrow \mathbb{C}$ is defined by

$$B_{\sigma, \zeta}((w, W), (v, V)) = \int_{\Omega} \sigma \nabla w \cdot \nabla v \, dx + \int_{\partial\Omega} \zeta(W - w)(V - v) \, dS. \quad (2.6)$$

Note that we intentionally exclude complex conjugations and work with bilinear forms instead of sesquilinear ones because such an approach simplifies certain expressions in what follows. Under the above assumptions, the potential pair $(u, U) \in \mathcal{H}^1$ is uniquely determined by (2.5) [28]. For physical justification of (2.2), see [15, 28].

The functional dependence of the electrode potentials on the conductivities and the applied electrode currents is denoted as $U(\sigma, \zeta; I) \in \mathbb{C}_\diamond^M$. In what follows, we employ a basis I_1, \dots, I_{M-1} for \mathbb{C}_\diamond^M as the electrode current patterns and adopt the notation

$$\mathcal{U}(\sigma, \zeta; I_1, \dots, I_{M-1}) = [U(\sigma, \zeta; I_1)^\top, \dots, U(\sigma, \zeta; I_{M-1})^\top]^\top \in \mathbb{C}^{M(M-1)}. \quad (2.7)$$

As the current basis is typically either clear from the context or unimportant for the presented arguments, the dependence of \mathcal{U} on I_1, \dots, I_{M-1} is often suppressed.

2.2. Derivatives of the CEM solution. We next consider the derivatives of the forward solution $(u, U) \in \mathcal{H}^1$ with respect to the conductivities and the electrode positions. For simplicity, let $\partial\Omega$ and ∂E be of class \mathcal{C}^∞ and assume the conductivities in (2.2) satisfy $\sigma \in L_+^\infty(\Omega) \cap \mathcal{C}^{0,1}(\overline{\Omega})$ and $\zeta \in \mathcal{Z} \cap H^1(\partial\Omega)$, although this level of regularity is not needed for all results presented in this section.¹ We refer to [30] for

¹In particular, it would be sufficient for all presented results to only assume that σ is Lipschitz continuous in some neighborhood of the boundary $\partial\Omega$.

careful analysis on the existence of the considered derivatives in the less regular case that ζ is piecewise constant and to [9, 28] for considerations on differentiation with respect to electrode positions when $\zeta \in H^1(\partial\Omega)$. Apart from assuming a smoother contact conductivity, the main difference to [30] is that we deduce more efficient computational formula for the mixed derivative with respect to the internal conductivity and the electrode positions. Since we consider the presented results straightforward, yet arguably tedious modifications of material in [28, 30], we do not present detailed proofs. Moreover, we do not claim that our regularity assumptions are optimal; the conditions on σ and its perturbations are required in [30] due to the discontinuities in ζ that make the derivatives with respect to the electrode positions singular in a certain sense [17].

To begin with, let us define how electrodes are moved along $\partial\Omega$. Let $a \in \mathcal{C}^1(E, \mathbb{R}^3)$ and define a perturbed set of electrodes via

$$E_m^a = \{P_x(x + a(x)) \mid x \in E_m\} \subset \partial\Omega, \quad m = 1, \dots, M, \quad (2.8)$$

where $P_x : \mathbb{R}^3 \supset B_\rho(x) \rightarrow \partial\Omega$ is the projection in the direction of $\nu(x)$ onto $\partial\Omega$, and $B_\rho(x)$ is an open ball of small enough radius $\rho > 0$ centered at x . The contact conductivity $\zeta : \partial\Omega \rightarrow \mathbb{C}$ is assumed to stretch accordingly, that is, the conductivity on the perturbed electrodes is defined via

$$\zeta^a(P_x(x + a(x))) = \zeta(x), \quad x \in E, \quad (2.9)$$

and it vanishes on $\partial\Omega \setminus \overline{E^a}$. It can be shown that there exists a constant $c = c(E, \Omega) > 0$ such that the definitions (2.8) and (2.9) are unambiguous if $\|a\|_{\mathcal{C}^1(E, \mathbb{R}^3)} < c$; see [17] for the proof of a closely related result. For a fixed set of electrodes E_1, \dots, E_M , we can now interpret the electrode potentials (as well as the interior potential) as a function of four variables, that is,

$$U : \begin{cases} (\sigma, \zeta, a, I) \mapsto U(\sigma, \zeta, a; I), \\ L_+^\infty(\Omega) \times \mathcal{Z} \times \mathcal{B}_c \times \mathbb{C}_\diamond^M \rightarrow \mathbb{C}_\diamond^M, \end{cases} \quad (2.10)$$

where $U(\sigma, \zeta, a; I)$ is the second part of the solution to (2.5) with E_1, \dots, E_M replaced by E_1^a, \dots, E_M^a , and \mathcal{B}_c denotes the origin-centered open ball of radius c in the topology of $\mathcal{C}^1(E, \mathbb{R}^3)$.

Let us then introduce the required derivatives. It is well known that the map $U : L_+^\infty(\Omega) \times \mathcal{Z} \times \mathcal{B}_c \times \mathbb{C}_\diamond^M \rightarrow \mathbb{C}_\diamond^M$ is Fréchet differentiable with respect to its first variable, but the same also holds for the second variable [18] although it is a less obvious result due to the fact that even an infinitesimally small perturbation can make the real part of the contact conductivity negative on some parts of the electrodes. These differentiability results, in fact, hold without more regularity than is assumed in Section 2.1. Let us start with the derivative with respect to the internal conductivity: The Fréchet derivative of U at $\sigma \in L_+^\infty(\Omega)$ in the direction $\eta \in L^\infty(\Omega)$, i.e., $D_\sigma U(\sigma; \eta) \in \mathbb{C}_\diamond^M$, is the second part of the unique solution $(D_\sigma u(\sigma; \eta), D_\sigma U(\sigma; \eta)) \in \mathcal{H}^1$ to

$$B_{\sigma, \zeta}((D_\sigma u(\sigma; \eta), D_\sigma U(\sigma; \eta)), (v, V)) = - \int_\Omega \eta \nabla u \cdot \nabla v \, dx \quad \text{for all } (v, V) \in \mathcal{H}^1, \quad (2.11)$$

where $(u, U) \in \mathcal{H}^1$ is the solution to (2.5). From the computational standpoint, it is important to note that this derivative can be assembled using the formula

(see, e.g., [29])

$$D_\sigma U(\sigma; \eta) \cdot \tilde{I} = - \int_{\Omega} \eta \nabla u \cdot \nabla \tilde{u} \, dx, \quad (2.12)$$

where $(\tilde{u}, \tilde{U}) \in \mathcal{H}^1$ is the solution to (2.5) for an auxiliary current pattern $\tilde{I} \in \mathbb{C}_{\diamond}^M$. In the following, all solutions for variational equations marked with \sim have \tilde{I} as the underlying electrode current pattern, and the ones without \sim are associated to I . The Fréchet derivative of U with respect to the contact conductivity allows a similar sampling formula [18],

$$D_\zeta U(\zeta; \omega) \cdot \tilde{I} = - \int_{\partial\Omega} \omega (U - u) (\tilde{U} - \tilde{u}) \, dS \quad (2.13)$$

for $\zeta \in \mathcal{Z}$ and a surface conductivity perturbation $\omega \in L^\infty(E)$.

The map $U : L_+^\infty(\Omega) \times \mathcal{Z} \cap H^1(\partial\Omega) \times \mathcal{B}_c \times \mathbb{C}_{\diamond}^M \rightarrow \mathbb{C}_{\diamond}^M$ is also Fréchet differentiable with respect to its third variable at the origin [17, 28]. The associated Fréchet derivative $D_a U(0; h)$ in the direction $h \in \mathcal{C}^1(E, \mathbb{R}^3)$ is defined by the second part of the unique solution $(D_a u(0; h), D_a U(0; h)) \in \mathcal{H}^1$ to

$$B_{\sigma, \zeta}((D_a u(0; h), D_a U(0; h)), (v, V)) = \int_{\partial\Omega} h_\tau \cdot \text{Grad}(\zeta) (U - u)(V - v) \, dS \quad (2.14)$$

for all $(v, V) \in \mathcal{H}^1$. Here h_τ is the tangential component of h and Grad is the surface gradient [16]. This derivative also allows a sampling formula similar to (2.12) and (2.13) for its efficient numerical evaluation, but it is omitted since it is not utilized in our numerical studies.

Let us finally consider the mixed derivative $D_a D_\sigma U$ that is a main building block in our OED algorithm. To be precise, we consider $D_\sigma D_a U$ without proving that the order of differentiation can be reversed. Moreover, we focus our attention on conductivity perturbations that are supported at a distance from $\partial\Omega$; this choice conveniently follows the material in [30], but such perturbations are also sufficient for our purposes because the ROI in our numerical experiments always lies in the brain tissue, i.e., in the interior of the computational head model. If we define

$$L_\delta^\infty(\Omega) = \{\kappa \in L^\infty(\Omega) \mid \text{dist}(\text{supp } \kappa, \partial\Omega) \geq \delta\}, \quad \delta > 0,$$

to be the space of admissible conductivity perturbations, the second Fréchet derivative $D_\sigma D_a U$ is well defined at $(\sigma, \zeta, 0, I)$ for any $(\sigma, \zeta, I) \in L_+^\infty(\Omega) \cap \mathcal{C}^{0,1}(\bar{\Omega}) \times \mathcal{Z} \cap H^1(\partial\Omega) \times \mathbb{C}_{\diamond}^M$. Moreover, it can be assembled via

$$\begin{aligned} D_\sigma D_a U(\sigma, \zeta, 0; \eta, h) \cdot \tilde{I} &= \int_{\partial\Omega} h_\tau \cdot \text{Grad}(\zeta) ((D_\sigma U(\sigma; \eta) - D_\sigma u(\sigma; \eta))(\tilde{U} - \tilde{u}) \\ &\quad + (U - u)(D_\sigma \tilde{U}(\sigma; \eta) - D_\sigma \tilde{u}(\sigma; \eta))) \, dS, \end{aligned} \quad (2.15)$$

where the perturbation directions satisfy $\eta \in L_\delta^\infty(\Omega)$ and $h \in \mathcal{C}^1(E, \mathbb{R}^3)$. The corresponding formula [30, (2.21)] for the case of piecewise constant contact conductivity can be deduced from (2.15) by noting that $h_\tau \cdot \text{Grad}(\zeta)$ corresponds to a weighted delta distribution on ∂E for a piecewise constant ζ .

A computational issue with (2.15) is that to evaluate $D_\sigma D_a U(\sigma, \zeta, 0; \eta, h)$ for all η corresponding to a discretization of the internal conductivity, the variational problem (2.11) must first be solved for each basis current and for as many right-hand sides as

there are degrees of freedom in the parametrization of $L^\infty_\delta(\Omega)$. On the other hand, (2.15) can be used to conveniently handle perturbations of the electrode positions as one simply needs to plug in (2.15) as many different h as there are admissible directions to which the electrodes can move. As the electrode positions are parametrized by their polar and azimuthal angles in our numerical experiments, there are only $2M$ ways to move the electrodes, which is significantly less than the number of basis functions in the parametrization of the conductivity perturbations. To conclude, it would thus be computationally advantageous to replace (2.15) by a formula that would not involve solving (2.11) for all conductivity perturbations but instead (2.14) for all admissible electrode perturbation directions.

For this reason, interpret the two terms on the right-hand side of (2.15) as right-hand sides for (2.14) with the test function pairs $(D_\sigma u(\sigma; \eta), D_\sigma U(\sigma; \eta))$ and $(D_\sigma \tilde{u}(\sigma; \eta), D_\sigma \tilde{U}(\sigma; \eta))$, respectively. By the symmetry of the bilinear form $B_{\sigma, \zeta} : \mathcal{H} \times \mathcal{H} \rightarrow \mathbb{C}$, this leads to

$$\begin{aligned} D_\sigma D_a U(\sigma, \zeta, 0; \eta, h) \cdot \tilde{I} &= B_{\sigma, \zeta}((D_\sigma \tilde{u}(\sigma; \eta), D_\sigma \tilde{U}(\sigma; \eta)), (D_a u(0; h), D_a U(0; h))) \\ &\quad + B_{\sigma, \zeta}((D_\sigma u(\sigma; \eta), D_\sigma U(\sigma; \eta)), (D_a \tilde{u}(0; h), D_a \tilde{U}(0; h))). \end{aligned}$$

The two terms on the right-hand side can now be interpreted as left-hand sides for (2.11), which finally yields the computationally more attractive formula

$$D_\sigma D_a U(\sigma, \zeta, 0; \eta, h) \cdot \tilde{I} = - \int_\Omega \eta (\nabla D_a u(0; h) \cdot \nabla \tilde{u} + \nabla u \cdot \nabla D_a \tilde{u}(0; h)) dx \quad (2.16)$$

for building a discretized version of the derivative $D_\sigma D_a U$.

2.3. Head model and computational implementation. We adopt the three-layer head model introduced in [9, 11], with the layers corresponding to the scalp, the highly resistive skull and the interior brain. The construction in [9, 11] models typical variations in the head anatomy over the human population by building a principal component model based on the library of 50 heads in [38]. However, here we restrict our attention to a single head anatomy, shown in Figure 2.1, without studying the effect of anatomical variations on the optimal electrode configurations. All electrodes shown in Figure 2.1 and employed in our numerical studies are discoidal in the sense that they are defined by intersections of the head surface with a circular cylinder of a given radius $R > 0$ and having its central axis aligned with the normal of the surface.

Before reviewing how a *finite element method* (FEM) can be used to approximate the solution for (2.5) and the derivatives of its second component with the help of (2.12), (2.13), (2.14) and (2.16), the choice of the perturbation vector field h in (2.14) must be considered. We follow the construction in [9]. An electrode position is parametrized by the polar $\theta_m \in (0, \pi/2)$ and azimuthal $\phi_m \in [0, 2\pi)$ angles of its center with respect to the midpoint of the bottom face of the head model in Figure 2.1. The tangent vectors for $\partial\Omega$ at the center x_m of E_m obtained by differentiating the parametrization of the head surface (cf. [9]) with respect to the polar and azimuthal angles are denoted by $\hat{\theta}_m, \hat{\phi}_m \in \mathbb{R}^3$, respectively.

We extend $\hat{\theta}_m$ as a constant vector field onto the whole electrode E_m and set

$$\tilde{h}_m^\theta(x) := (\hat{\theta}_m(x))_\tau, \quad x \in E_m,$$

to be its tangential component. To ensure that all points on E_m move as much in the tangential direction so that the area of the electrode is approximately conserved, we

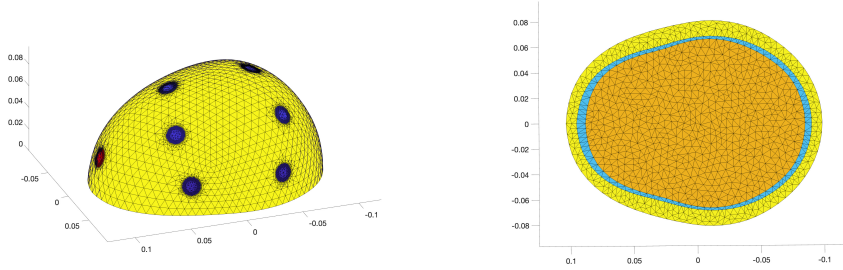


Fig. 2.1: A finite element discretization of the sample head anatomy used in our numerical studies. Left: the surface of the head model with a set of electrodes. Right: the bottom of the computational model showing the skin, skull and brain layers. The unit of length is meter.

apply a scaling

$$h_m^\theta(x) := \frac{|\tilde{h}_m^\theta(x_m)|}{|\tilde{h}_m^\theta(x)|} \tilde{h}_m^\theta(x), \quad x \in E_m,$$

with $|\cdot|$ denoting the Euclidean norm, and finally extend h_m^θ as zero on to the other electrodes. Although the perturbation of E_m by such a vector field h_m^θ in the spirit of (2.8) does not exactly maintain the shape of the electrode E_m , it seems feasible that the variations in its size are small compared to the moved distance for a regular spherical surface and small electrodes depicted in Figure 2.1. A perturbation vector field h_m^ϕ corresponding to the azimuthal angle of the center for E_m is constructed in an equivalent manner. The derivatives of solutions to (2.5) with respect to the polar or the azimuthal angle of an electrode E_m are approximated by solving (2.14) with $h = h_m^\theta$ or $h = h_m^\phi$, respectively, for $(D_a u(0; h), D_a U(0; h))$.

In order to parametrize the dependence of the solution to (2.5) on the contact conductivity, we assume the contact takes a common fixed form on each electrode. To be more precise, following [9, Section 4.2], we define the restriction of ζ to E_m , $m = 1, \dots, M$, as

$$\zeta|_{E_m}(r_m, \omega_m) = \zeta_m \hat{\zeta}(r_m, \omega_m), \quad r_m \in [0, R), \quad \omega_m \in [0, 2\pi), \quad (2.17)$$

in the polar coordinates (r_m, ω_m) induced by orthogonally projecting the electrode onto a cross-section of the circular cylinder defining it. As in [9], the shape of an individual contact is defined by the smooth function

$$\hat{\zeta}(r, \omega) = \exp\left(\tau - \frac{\tau R^2}{R^2 - r^2}\right)$$

that vanishes to infinite order at $|r| = R$. In our numerical experiments, the value $\tau = 0.4$ is used for the shape parameter. The free parameter $\zeta_m \in \mathbb{C}$, with $\text{Re } \zeta_m > 0$, in (2.17) defines the net conductance on E_m . In what follows, we abuse the notation by identifying the contact conductance function with the vector $\zeta = [\zeta_1, \dots, \zeta_M]^\top \in \mathbb{C}_+^M$, where \mathbb{C}_+ denotes the open right half of the complex plain.

In the rest of this work, we consider a discretized version of (2.5) by parametrizing the conductivity σ as

$$\sigma = \sum_{j=1}^N \sigma_j \varphi_j, \quad (2.18)$$

where $\sigma_j \in \mathbb{C}_+$ and $\varphi_j \in H^1(\Omega)$, $j = 1, \dots, N$, are the piecewise linear basis functions corresponding to a *finite element* (FE) mesh of Ω .² We refer to [9, 11] for more information on the construction of tetrahedral FE meshes such as shown in Figure 2.1. We denote by σ both the vector $\sigma \in \mathbb{C}_+^N$ and the corresponding conductivity defined by (2.18); such an identification between linear combinations of the FE basis functions and vectors of \mathbb{C}^N is employed throughout this text. By the solution (u, U) of (2.5) we mean from here on the approximate FE solution in the subspace

$$\text{span}\{\varphi_j\}_{j=1}^N \oplus \mathbb{C}_\diamond^M \subset H^1(\Omega) \oplus \mathbb{C}_\diamond^M;$$

consult, e.g., [49, 50] for the implementation details.

Summarizing the above developments, we (re)define a finite-dimensional forward map

$$\mathcal{U} : \begin{cases} (\sigma, \zeta, \theta, \phi) \rightarrow \mathcal{U}(\sigma, \zeta, \theta, \phi), \\ \mathbb{C}_+^N \times \mathbb{C}_+^M \times (0, \pi/2)^M \times [0, 2\pi)^M \rightarrow \mathbb{C}^{M(M-1)} \end{cases} \quad (2.19)$$

that is a discretized version of (2.7) with the dependence on the electrode angles explicitly accounted for. The Jacobian of $J_\sigma = J_\sigma(\sigma, \zeta, \theta, \phi) \in \mathbb{C}^{M(M-1) \times N}$ with respect to $\sigma \in \mathbb{C}_+^N$ can be computed by letting η run through the FE basis functions in (2.12) for all I and \tilde{I} in the employed current basis. Similarly, the Jacobian $J_\zeta = J_\zeta(\sigma, \zeta, \theta, \phi) \in \mathbb{C}^{M(M-1) \times M}$ with respect to $\zeta \in \mathbb{C}_+^M$ can be assembled by choosing ω in (2.13) to be of the form (2.17) with ζ going through the standard basis vectors of \mathbb{C}^M . Finally, the elementwise derivatives

$$\frac{\partial(J_\sigma)_{ij}}{\partial\theta_m}(\sigma, \zeta, \theta, \phi) \quad \text{and} \quad \frac{\partial(J_\sigma)_{ij}}{\partial\phi_m}(\sigma, \zeta, \theta, \phi) \quad (2.20)$$

for $i = 1, \dots, M(M-1)$, $j = 1, \dots, N$ and $m = 1, \dots, M$, needed in the OED algorithm for the linearized model, are approximated by setting $h = h_m^\theta$ or $h = h_m^\phi$ on the right-hand side of (2.16), choosing $\eta = \varphi_j$, setting the current pattern I to be the one corresponding to the index i in $\mathcal{U}(\sigma, \zeta, \theta, \phi)$ (cf. (2.7)), and letting \tilde{I} run through the whole current basis of \mathbb{C}_\diamond^M .

Let us then assume the knowledge of background conductivity levels $\sigma_0 \in \mathbb{C}_+^N$ and $\zeta_0 \in \mathbb{C}_+^M$. In the stroke monitoring framework, the former would be based on information on the physiology of the patient, whereas the latter would correspond to empirical information on the expected quality of electrode contacts. We resort to linearizing the map $\mathcal{U} : \mathbb{C}_+^N \times \mathbb{C}_+^M \times (0, \pi/2)^M \times [0, 2\pi)^M \rightarrow \mathbb{C}^{M(M-1)}$ with respect to either its first or both its first and second variables. Assuming a noiseless measurement $\mathcal{V} \in \mathbb{C}^{M(M-1)}$ and performing the linearization with respect to both σ and ζ leads to the approximate measurement model

$$\mathcal{U}(\sigma_0, \zeta_0) + J_\sigma(\sigma_0, \zeta_0)(\sigma - \sigma_0) + J_\zeta(\sigma_0, \zeta_0)(\zeta - \zeta_0) = \mathcal{V},$$

where the dependence of the Jacobians on the design parameters θ and ϕ has been suppressed for brevity. Denoting $\kappa = \sigma - \sigma_0$, $\xi = \zeta - \zeta_0$, $y = \mathcal{V} - \mathcal{U}(\sigma_0, \zeta_0)$,

$$J = [J_\sigma(\sigma_0, \zeta_0), J_\zeta(\sigma_0, \zeta_0)] \quad \text{and} \quad w = \begin{bmatrix} \kappa \\ \xi \end{bmatrix}, \quad (2.21)$$

²In fact, the basis functions φ_j and their number N change when electrodes move on $\partial\Omega$ due to remeshing.

we arrive at the model

$$Jw = y \quad (2.22)$$

that is further analyzed from Bayesian standpoint in the next section.

When considering the actual problem of OED, we assume that ζ_0 is a good enough estimate for the contacts and set $J = J_\sigma$ and $w = \kappa$ in (2.22). That is, the complete linearized model (2.22) is only considered when computing reconstructions with the TV prior by the algorithm based on the lagged diffusivity iteration. The reason for this choice is two-fold: we do not expect the dependence of the model on ζ to severely affect the optimal designs aiming at reconstructing σ and we want to avoid introducing extra technical material in the form of another second derivative $D_\zeta D_a U$ in addition to $D_\sigma D_a U$. In the following, we denote the design variables by $d = (\theta, \phi)$ and stress that $J = J(d)$.

3. Bayesian inversion. In this section, we first describe a fully Gaussian probabilistic version of the linearized model (2.22), with the dependence on the contact conductivity suppressed. Subsequently, a smoothed TV prior and the lagged diffusivity iteration are considered. For the rest of this text, we assume for simplicity that all variables are real-valued.

3.1. A fully Gaussian model for OED. Let us consider a probabilistic version of (2.22) with the dependence on the contact conductivity ignored:

$$Y = J_\sigma W + E, \quad (3.1)$$

where the measurement data $Y \in \mathbb{R}^{M(M-1)}$ and the unknown *internal* conductivity perturbation $W \in \mathbb{R}^N$ are interpreted as independent random variables. The additive noise process E is assumed to be a zero-mean Gaussian with a symmetric positive-definite covariance matrix $\Gamma_{\text{noise}} \in \mathbb{R}^{M(M-1) \times M(M-1)}$.

Let us assume that *a priori* $W \sim \mathcal{N}(0, \Gamma_{\text{prior}})$, where the prior covariance $\Gamma_{\text{prior}} \in \mathbb{R}^{N \times N}$ is also symmetric and positive definite. In such a case, it is well known that the posterior density $\pi(w | y)$ is a Gaussian as well (see, e.g., [31]), with the covariance

$$\Gamma_{\text{post}} = \Gamma_{\text{prior}} - \Gamma_{\text{prior}} J_\sigma^\top (J_\sigma \Gamma_{\text{prior}} J_\sigma^\top + \Gamma_{\text{noise}})^{-1} J_\sigma \Gamma_{\text{prior}} \quad (3.2)$$

and the mean

$$\hat{w} = \Gamma_{\text{prior}} J_\sigma^\top (J_\sigma \Gamma_{\text{prior}} J_\sigma^\top + \Gamma_{\text{noise}})^{-1} y. \quad (3.3)$$

In particular, the posterior covariance does not depend on the measured data y , and thus an optimal design aiming to make the posterior as localized as possible can be sought offline, i.e., prior to taking any measurements.

In our numerical experiments on OED for the head model, a weighted trace of the posterior covariance $\Gamma_{\text{post}} = \Gamma_{\text{post}}(d)$ is minimized with respect to the design variable d . Note that the dependence of Γ_{post} on d is inherited from that of $J_\sigma = J_\sigma(d)$. The prior covariance in (3.2) originates either from *a priori* assumption on the conductivity perturbation, or it is a byproduct of a reconstruction algorithm based on sequential linearizations and the lagged diffusivity iteration, as described in the following section.

3.2. Total variation prior and lagged diffusivity. Let us then assume that the prior density is of the form

$$\pi(w) = \exp(-\gamma \Phi(\kappa)), \quad (3.4)$$

where

$$\Phi(\kappa) = \int_{\Omega} v(x) \varphi(|\nabla \kappa|) dx, \quad \text{with } \varphi(t) = \sqrt{t^2 + T^2} \approx |t|, \quad (3.5)$$

accompanied by the information that the interior conductivity perturbation κ vanishes on $\partial\Omega$. As in [10], $v : \Omega \rightarrow \mathbb{R}_+$ is the reciprocal of a smooth cut-off function,

$$v(x) = \left(\frac{1}{2} (1 + \tanh(c_v(\text{dist}(x, \partial\Omega) - b_v))) \right)^{-1}, \quad x \in \Omega, \quad (3.6)$$

where $c_v > 0$ and $b_v > 0$ are chosen so that the value of v is large in the skin layer and decreases to almost one within the skull layer. The role of v in the prior is to encode the assumption that a stroke mainly causes conductivity changes in the brain tissue, but in the computational experiments it also mitigates the tendency of electrodes to approach the bottom face of the head model because v also makes changes in the conductivity improbable in the lower parts of the brain. Note that the vector of perturbations in the peak values of the contact conductivity, ξ , is assumed to have an uninformative prior, which explains why ξ does not appear on the right-hand side of (3.4). In particular, the dependence of the linearized model (2.22) on ξ is not ignored in this section. We assume that there are $N' < N$ interior nodes in the employed FE mesh and identify κ in the rest of this section with an element of $\mathbb{R}^{N'}$, instead of one in \mathbb{R}^N .

Let us continue to assume a zero-mean Gaussian noise model that is independent of W and follow the treatment in [24]. The quest for a MAP estimate for the linearized model (2.22) leads now to considering a nonquadratic Tikhonov functional

$$\frac{1}{2} (y - Jw)^\top \Gamma_{\text{noise}}^{-1} (y - Jw) + \gamma \Phi(\kappa). \quad (3.7)$$

The necessary condition for a minimizer of (3.7) is (cf. (2.21))

$$J^\top \Gamma_{\text{noise}}^{-1} Jw + \gamma \begin{bmatrix} (\nabla_{\kappa} \Phi)(\kappa) \\ 0 \end{bmatrix} = J^\top \Gamma_{\text{noise}}^{-1} y, \quad (3.8)$$

where $0 \in \mathbb{R}^M$. Utilizing the identification of vectors in $\mathbb{R}^{N'}$ with elements of $H_0^1(\Omega)$ via the employed FE basis, it is straightforward to check that

$$(\nabla_{\kappa} \Phi)(\kappa) = \Theta(\kappa) \kappa, \quad (3.9)$$

where the multiplier matrix $\Theta(\kappa)$ is given elementwise as

$$\Theta_{i,j}(\kappa) := \int_{\Omega} \frac{v(x)}{\sqrt{|\nabla_x \kappa(x)|^2 + T^2}} \nabla \varphi_i(x) \cdot \nabla \varphi_j(x) dx, \quad i, j = 1, \dots, N'.$$

As reasoned in [24], the invertibility of $\Theta(\kappa)$ for any $\kappa \in \mathbb{R}^{N'}$ is guaranteed via an interpretation as a FE system matrix originating from a discretization of an elliptic differential operator combined with a homogeneous Dirichlet boundary condition.

Plugging the presentation (3.9) in (3.8) and expanding gives

$$\begin{bmatrix} J_{\sigma}^\top \Gamma_{\text{noise}}^{-1} J_{\sigma} + \gamma \Theta(\kappa) & J_{\sigma}^\top \Gamma_{\text{noise}}^{-1} J_{\zeta} \\ J_{\zeta}^\top \Gamma_{\text{noise}}^{-1} J_{\sigma} & J_{\zeta}^\top \Gamma_{\text{noise}}^{-1} J_{\zeta} \end{bmatrix} w = \begin{bmatrix} J_{\sigma}^\top \\ J_{\zeta}^\top \end{bmatrix} \Gamma_{\text{noise}}^{-1} y. \quad (3.10)$$

Denoting $B_\sigma = \Gamma_{\text{noise}}^{-1/2} J_\sigma$, $B_\zeta = \Gamma_{\text{noise}}^{-1/2} J_\zeta$ and solving the second row of (3.10) for ξ gives

$$\xi = (B_\zeta^\top B_\zeta)^{-1} B_\zeta^\top (\Gamma_{\text{noise}}^{-1/2} y - B_\sigma \kappa). \quad (3.11)$$

Substituting this for ξ on the first row of (3.10) results in the formula

$$(A^\top A + \gamma \Theta(\kappa)) \kappa = A^\top b, \quad (3.12)$$

where

$$A = Q B_\sigma \quad \text{and} \quad b = Q \Gamma_{\text{noise}}^{-1/2} y,$$

with $Q = I - B_\zeta (B_\zeta^\top B_\zeta)^{-1} B_\zeta^\top$ being the orthogonal projection onto the orthogonal complement of the range of B_ζ in $\mathbb{R}^{M(M-1)}$. Here and in what follows, an identity matrix of an appropriate size is denoted by I .

The idea is now to solve (3.12) by means of the lagged diffusivity iteration [13, 19, 51], which can be interpreted to produce a Gaussian approximation for the posterior of κ as its byproduct [5, 8, 26]. Start from an initial guess $\kappa^0 = 0$ for the solution of (3.12). Assuming to have $\kappa^{(j)}$ in hand, $\Theta(\kappa)$ is replaced in (3.12) by $\Theta(\kappa^{(j)})$, which yields a linear equation for κ . The solution of this equation is the mean of the Gaussian posterior defined by the model for $A\kappa = b$, assuming a zero-mean Gaussian prior for κ with the inverse covariance matrix $\gamma \Theta(\kappa^{(j)})$ and an additive white noise model [31]. Using the Woodbury matrix identity (cf. (3.2)–(3.3)), the mean and the covariance of this posterior allow the representations

$$\kappa^{(j+1)} = \Theta(\kappa^{(j)})^{-1} A^\top (\gamma I + A \Theta(\kappa^{(j)})^{-1} A^\top)^{-1} b \quad (3.13)$$

and

$$\Gamma^{(j+1)} = \gamma^{-1} \left(\Theta(\kappa^{(j)})^{-1} - \Theta(\kappa^{(j)})^{-1} A^\top (\gamma I + A \Theta(\kappa^{(j)})^{-1} A^\top)^{-1} A \Theta(\kappa^{(j)})^{-1} \right), \quad (3.14)$$

respectively.

The iteration (3.13) is terminated after a predefined stopping criterion is satisfied. The final posterior mean and covariance, say, $\kappa^{(J)}$ and $\Gamma^{(J)}$, then define a Gaussian density that can be used in choosing new positions for the electrodes as explained in Section 4. Note that the iteration defined by (3.13) is not overly expensive computationally because A has only $M(M-1)$ rows and operating with the inverse of the sparse matrix $\Theta(\kappa^{(j)})$ that originates from a FE discretization can be performed efficiently. Moreover, the covariance matrix in (3.14) only needs to be computed at the final iteration, since (3.13) is independent of (3.14). After computing a MAP estimate for the posterior by the above scheme, the peak values of the contact conductivity perturbation could be updated according (3.11) with $\kappa = \kappa^{(J)}$.

REMARK 3.1. *In the numerical experiments of Section 5, we compute the TV-based reconstructions by combining the lagged diffusivity iteration with sequential linearizations of the forward model. That is, once a conductivity perturbation pair, say, $w_k = (\kappa_k, \xi_k)$, has been computed by the above iteration, the forward model is re-linearized at the corresponding new base point $(\sigma_k, \zeta_k) = (\sigma_0 + \kappa_k, \zeta_0 + \xi_k)$ and the lagged diffusivity iteration is once again applied to the nonquadratic Tikhonov functional corresponding to the negative log-likelihood for the TV prior. The unknown*

$(\kappa_{k+1}, \xi_{k+1})$ that is sought for in the new round of iteration still corresponds to a deviation from the background level (σ_0, ζ_0) , which means that one must redefine

$$y = \mathcal{V} - \mathcal{U}(\sigma_k, \zeta_k) + J_\sigma(\sigma_k, \zeta_k)\kappa_k + J_\zeta(\sigma_k, \zeta_k)\xi_k + e$$

in the analysis of this section, with e denoting the considered realization of the additive measurement noise process E . The reason for this choice is that it is natural to assume the TV prior for the change in the internal conductivity compared to the original background level σ_0 , not compared to the latest reconstruction σ_k . Once the nested iterations corresponding to the sequential linearizations and the lagged diffusivity argument have been terminated, the final approximate Gaussian posterior covariance for the perturbation from the background conductivity σ_0 can be used for choosing new electrode positions as explained in the next section. See [10, 24] for previous applications of such a reconstruction algorithm to EIT, with the difference that utilizing the Woodbury matrix formula for (3.13) is in [10, 24] replaced by a certain priorconditioned LSQR iteration and the Morozov discrepancy principle.

4. Optimal experimental design. In this section, we briefly describe the concept of A-optimality in our setting and consider numerically solving the associated optimization problems. We refer to [2, 12] for more information on Bayesian OED and to [40] for material on numerical optimization.

4.1. A-optimality. Assume that the forward model has been linearized around a given internal background conductivity and that the prior information on the conductivity perturbation is given in the form of a zero-mean Gaussian prior with a covariance matrix Γ_{prior} . In other words, we assume the setting of Section 3.1. The prior information may originate from one of two sources:

1. A Gaussian prior is directly assumed for the linearized model, and the computations are performed offline in a nonadaptive manner.
2. The algorithm based on sequential linearizations, a TV prior and the lagged diffusivity iteration, described in Section 3.2, is first applied to measurements on an initial electrode configuration. After the algorithm has been terminated, the covariance of the final Gaussian approximation for the internal conductivity perturbation is dubbed Γ_{prior} .

In both cases, the covariance Γ_{post} of the Gaussian posterior for the linearized model is given by (3.2). The A-optimality criterion corresponds to minimizing the trace of a weighted version of this covariance:

$$d_A = \arg \min_d \Psi_A(d), \quad \text{with } \Psi_A(d) := \text{tr}(\mathcal{A}\Gamma_{\text{post}}(d)\mathcal{A}^\top) = \text{tr}(\mathcal{A}^\top\mathcal{A}\Gamma_{\text{post}}(d)), \quad (4.1)$$

where the last equality follows from a cyclic property of the matrix trace. In other words, an A-optimal design d_A minimizes the expected squared distance of the unknown from the posterior mean in the seminorm defined by the positive semidefinite matrix $\mathcal{A}^\top\mathcal{A}$; see, e.g., [7]. In our setting, the weighing provided by \mathcal{A} for the diagonal elements of Γ_{post} is essential as they correspond to the nodal values of FE basis functions with supports of different sizes. To be able to measure distances in the squared $L^2(\Omega)$ norm, the proper choice for $\mathcal{A}^\top\mathcal{A}$ is thus the mass matrix corresponding to the used FE basis; see, e.g., [23]. Moreover, if only a certain ROI inside the head model is considered, as is often the case in our numerical tests, the FE basis functions corresponding to the nodes outside the ROI are replaced by zero functions when forming the mass matrix.

Algorithm 1 (Gradient descent)

Choose a tolerance $\epsilon > 0$, an initial guess d_0 , the maximum number of iterations N_{GD} , and a step size parameter $\lambda > 0$. Initialize $i = 0$.

while $|\nabla\Psi_A(d_i)| > \epsilon$ and $i < N_{\text{GD}}$ **do**

- ▷ Compute the search direction $q = \tilde{q}/|\tilde{q}|$, with $\tilde{q} = -\nabla\Psi_A(d_i)$.
- ▷ Select the step size $\bar{\lambda}$ based on Algorithm 2 with an initial guess λ .
- ▷ Set $d_{i+1} = d_i + \bar{\lambda}q$.
- ▷ Update $i = i + 1$.

end while

return d_i

Algorithm 2 (Inexact line search with Armijo's rule)

Choose the maximum number of iterations N_{Armijo} and scaling parameters $\alpha, \beta \in (0, 1)$. Initialize a counter as $l = 0$. The initial step size $\lambda > 0$, the considered base point d_i , and the search direction q are given as inputs.

while $l < N_{\text{Armijo}}$ **do**

- if** $\Psi_A(d_i + \lambda q) - \Psi_A(d_i) < \lambda\alpha\nabla\Psi_A(d_i)^\top q$ **then**

 - ▷ Return $\bar{\lambda} = \lambda$.

- else**

 - ▷ Set $\lambda = \beta\lambda$.

- end if**
- ▷ Set $l = l + 1$.

end while

return $\bar{\lambda} = \lambda$

When visualizing the evolution of the A-optimality target during its minimization, instead Ψ_A itself, the value of $\tilde{\Psi}_A = \Psi_A^{1/2}$ is monitored. With the above choice for the weight \mathcal{A} , the value of $\tilde{\Psi}_A$ is the square root of the expected squared L^2 error over the ROI under the linearized measurement model.

4.2. Minimization of the A-optimality target. The minimization of the A-optimality target Ψ_A is performed with gradient descent accompanied by an inexact line search based on Armijo's rule; see, e.g., [40]. The complete minimization algorithm is given as a combination of Algorithms 1 and 2.

Observe that in (3.2), only the Jacobian matrix $J_\sigma = J_\sigma(d)$ depends on the design parameter vector d that determines the positions of the electrodes. The elementwise derivatives of $J_\sigma(d)$ can be approximated using (2.20). Hence, the derivatives of the optimization target $\Psi_A(d)$ needed in Algorithm 1 can also be computed straightforwardly, yet tediously, by applying (2.20) and well-known matrix differentiation formulas to (3.2) and (4.1). However, we do not stress this matter any further here, but simply assume that we have access to an approximation of the gradient of Ψ_A when running Algorithms 1 and 2.

REMARK 4.1. *When the polar angle θ_m of the center of the electrode E_m is small, i.e., the electrode lies close to the ‘north pole’ of the head model, the derivative with respect to the azimuthal angle ϕ_m of the center of E_m in Algorithms 1 and 2 is not used to update the azimuthal angle itself but the projected position of the electrode center along a straight line on the tangent plane touching the head model at the north pole. The reason for this is to prevent electrodes with small polar angles from rotating*

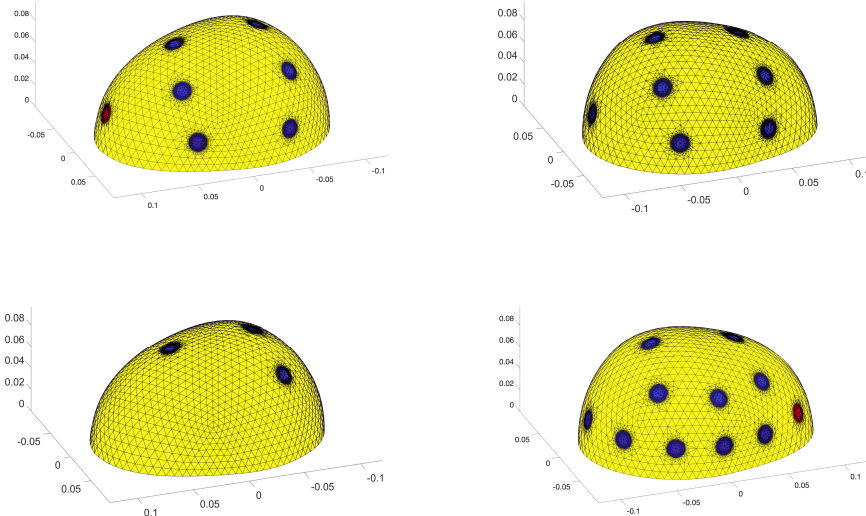


Fig. 5.1: The employed initial configurations with $M = 12$ electrodes. The feeding electrode is shown in red. Top: a symmetric initial electrode configuration from two perspectives. Bottom: an initial electrode configuration concentrated close to the ROI or stroke in the right posterior quadrant of the brain from two perspectives.

around the north pole during the optimization process.

5. Numerical experiments. The computations are performed on the three-layer head model presented in Figure 2.1. The employed FE meshes, used for discretizing both the conductivity and the first component of a solution to (2.5), have approximately $N = 15\,000$ nodes and 70 000 tetrahedra with appropriate refinements at the electrodes. The precise characteristics of the mesh depend on the positions of the electrodes on the surface of the head. However, when the positions of the electrodes are altered, the mesh only changes in the skin and skull layers, i.e., the mesh for the brain is the same in all computations. The needed FE meshes are formed using an updated version of the workflow introduced in [9, 11], with emphasis on the robustness of meshing when electrodes are close to each other or near the bottom edge of the head model.

The number of electrodes is chosen to be $M = 12$ in all numerical experiments, and their common radius is set to 7.5 mm. Denoting the l th Cartesian basis vector by e_l , the employed current basis are $I_m = e_1 - e_{m+1}$, $m = 1, \dots, M - 1$, that is, the same electrode always feeds the current into the head and it flows out in turns through the other $M - 1$ electrodes. In the numerical tests, we consider the two initial configurations for the electrodes shown in Figure 5.1, with the current feeding electrodes marked in red. Although the effect of the initial position for the feeding electrode is briefly discussed in Section 5.1, we refrain from further analysis on the role of the current patterns and settle for referring to [32, 33] for their optimization in the Bayesian framework.

The peak values of the contact conductances are assumed to be known and set to $\zeta_1, \dots, \zeta_M = 10^3 \text{ S/m}^{-2}$, which corresponds to good contacts in the framework

of the smoothed CEM; see [28, Section 4.3]. For the lagged diffusivity iteration with the smoothed TV prior in Section 3.2 this means that the linearization of the forward model is always performed at the correct value of ζ ; in the terminology of Remark 3.1, the update formula (3.11) is not utilized, but one simply sets $\xi_k = 0$. Although it is not realistic to assume the contact conductances are known in a practical measurement setup for EIT, we have decided to reduce their role in our numerical tests to enable concentrating on the effect the head geometry and the location of the ROI or a stroke have on the A-optimized electrode positions. The conductivities of healthy skin, skull and brain tissues are chosen as 0.2 S/m, 0.06 S/m and 0.2 S/m, respectively (cf. [21, 35, 37, 39, 41]).

The zero-mean Gaussian measurement noise is assumed to have a diagonal covariance matrix of the form $\eta^2 \mathbf{I}$, where the standard deviation is defined to be

$$\eta = \omega \left(\max \mathcal{U}(\sigma, \zeta; I_1, \dots, I_{M-1}) - \min \mathcal{U}(\sigma, \zeta; I_1, \dots, I_{M-1}) \right). \quad (5.1)$$

Here, max and min operations are taken over the components of the complete measurement vector $\mathcal{U} \in \mathbb{R}^{M(M-1)}$, the conductivity σ is defined by the background levels for the three-layer head model, and the current patterns are those for the symmetric initial electrode configuration shown on the first row of Figure 5.1. We choose the value $\omega = 10^{-3}$ for the free scaling parameter and keep the noise covariance matrix fixed throughout the numerical studies.

The free parameters in Algorithms 1 and 2 are set to $\epsilon = 0$, $N_{\text{GD}} = 40$, $\lambda = 0.5$, $N_{\text{Armijo}} = 30$, $\alpha = 1/2$ and $\beta = 5/6$. In particular, we always simply run Algorithm 1 for 40 rounds without considering stopping it earlier because the effect of numerical errors makes it difficult to reliably infer whether a local minimum has been reached. The choices of ϵ , λ , α and β have an effect on the performance of the optimization routine, but this aspect is not further analyzed here.

5.1. Gaussian prior with a region of interest. Let us start with a Gaussian prior for the conductivity perturbation, which allows offline minimization for the A-optimality target Ψ_A in our linearized setting. The prior covariance is given elementwise as

$$(\Gamma_{\text{prior}})_{i,j} = \varsigma^2 \exp \left(-\frac{|x_i - x_j|^2}{2\ell^2} \right), \quad (5.2)$$

where $\ell = 0.05$ is the assumed correlation length, $\varsigma = 0.2$ is the pixelwise standard deviation, and x_i and x_j are the coordinates of the nodes with indices i and j in the FE mesh.

The first numerical test assumes the ROI is the intersection of the brain with the half-space $\{x \in \mathbb{R}^3 \mid x_3 \geq 0.02\}$. The initial and optimized electrode configuration are shown on the top row of Figure 5.1 and in Figure 5.2, respectively. The electrodes have reorganized themselves but not moved much in total, which is not surprising since the initial measurement configuration and the ROI are both symmetric. Be that as it may, the evolution of $\tilde{\Psi}_A$ plotted in the bottom right image of Figure 5.2 reveals a decrease of 3.67% during the minimization process. If the feeding electrode in the initial configuration on the top row of Figure 5.1 and in the setup of Figure 5.2 is chosen to be another electrode, the reduction in the value of $\tilde{\Psi}_A$ when switching from the initial configuration to the one in Figure 5.2 is still 3.14–3.80% depending on the chosen feeding electrode. Take note that the optimization algorithm is not rerun to deduce these numbers, but the index of the current-feeding electrode is simply

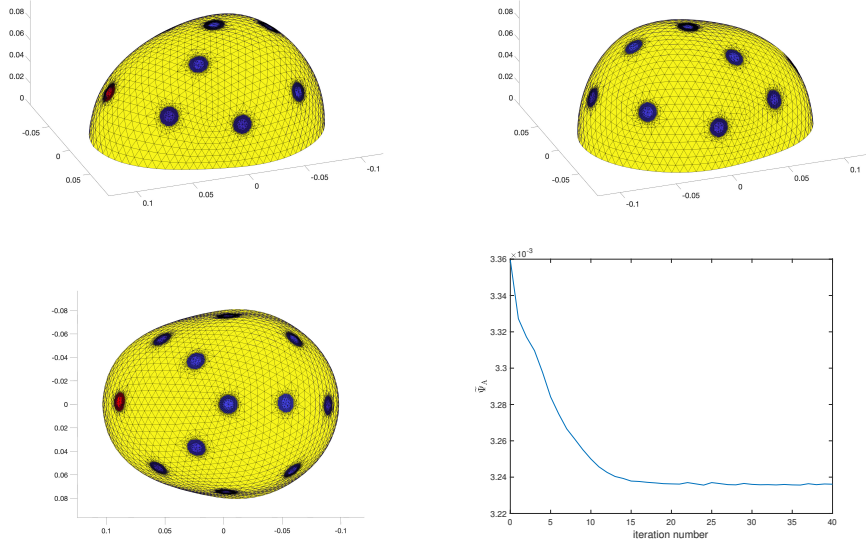


Fig. 5.2: Gaussian Test 1. The ROI is the brain with its bottom layer of height 2 cm excluded. Top and bottom left: the optimized electrode setup deduced by starting from the symmetric initial configuration of Figure 5.1. Bottom right: the evolution of $\tilde{\Psi}_A$ during the application of Algorithm 1.

chosen to go through all other options when evaluating $\tilde{\Psi}_A$ for the two electrode configurations. Although the choice of the feeding electrode has an effect on the A-optimal configuration, optimizing the configuration for a fixed feeding electrode thus seems to reduce the value of the A-optimality target for other choices of the feeding electrode as well — at least for the considered parameter values.

In the second test the ROI is chosen to be the intersection of the brain with the three half spaces

$$\{x \in \mathbb{R}^3 \mid x_3 \geq 0.02\}, \quad \{x \in \mathbb{R}^3 \mid x_1 \leq 0\}, \quad \{x \in \mathbb{R}^3 \mid x_2 \leq 0\}.$$

In other words, it is essentially the right posterior quadrant of the brain, which could, e.g., reflect one’s knowledge on the position of the stroke based on a CT image. The top and bottom rows of Figure 5.3 illustrate the optimized electrode positions starting from the top and bottom initial configurations in Figure 5.1, respectively. For both initial configurations, the minimization algorithm moves most of the electrodes to the vicinity of the right posterior quadrant of the brain, with a couple of electrodes, including the feeding one, situated at a longer distance from the ROI. Although qualitatively similar, the optimized configurations are not precisely the same, which may be caused by local minima or numerical inaccuracies in the evaluation of Ψ_A and its derivatives during the minimization process.

Figure 5.4 shows the evolution of $\tilde{\Psi}_A$ during Algorithm 1 for the considered two initial configurations. The initial electrode setup that is concentrated in the vicinity of the ROI leads to a slightly, i.e., 1.30%, lower minimized value for $\tilde{\Psi}_A$. However, the difference in the corresponding initial values for $\tilde{\Psi}_A$ is significant: the square root of the expected squared L^2 reconstruction error over the ROI for the symmetric initial configuration is 15.08% higher than that for the initial configuration accounting for

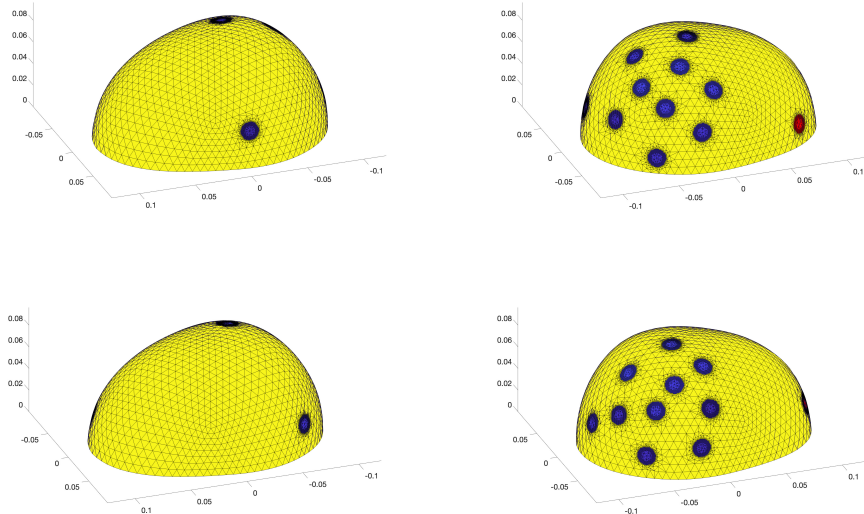


Fig. 5.3: Gaussian Test 2. The ROI is the right posterior quadrant of the brain with its bottom layer of height 2 cm excluded. Top: the optimized electrode setup deduced by starting from the symmetric initial configuration on the top row of Figure 5.1. Bottom: the optimized electrode setup deduced by starting from the pre-optimized initial configuration on the bottom row of Figure 5.1.

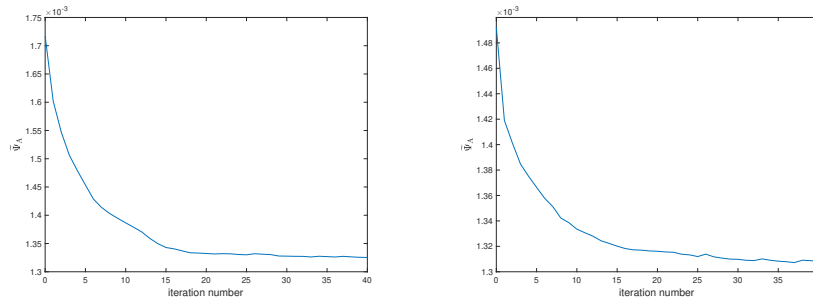


Fig. 5.4: Gaussian Test 2. The evolution of $\tilde{\Psi}_A$ during Algorithm 1 when the ROI is the right posterior quadrant of the brain. Left: the symmetric initial configuration on the top row of Figure 5.1. Right: the pre-optimized initial configuration on the bottom row of Figure 5.1.

the location of the ROI to a certain extent. This demonstrates that the intuition of placing most available electrodes close to the ROI seems correct. For the symmetric initial configuration, running Algorithm 1 resulted in a reduction of 22.82% in the value of $\tilde{\Psi}_A$, whereas the reduction was only 12.34% for the ‘pre-optimized’ initial configuration.

5.2. Total variation with an inclusion. Assume there is a spherical conductive anomaly of radius 1.8 cm in the right posterior quadrant of the brain as illustrated in Figure 5.5. The inhomogeneity could model a hemorrhagic stroke [47]. We first measure (i.e., simulate) noisy data (cf. (5.1)) with an initial electrode configu-

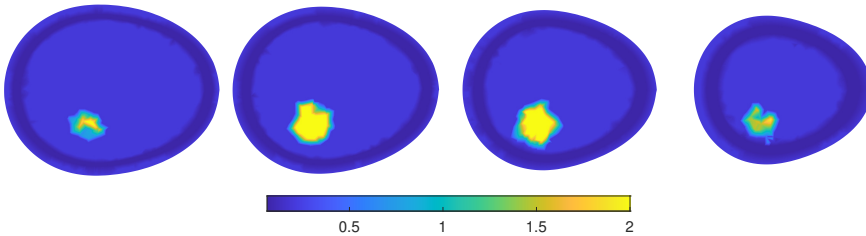


Fig. 5.5: Cross-sections of the investigated head model with a spherical conductive inclusion in the right posterior quadrant of the brain. The horizontal slices are at heights 3 cm, 4 cm, 5 cm and 6 cm. The unit of conductivity is S/m.

ration and then compute a reconstruction corresponding to a smoothed TV prior by combining lagged diffusivity iteration with sequential linearizations, as explained in Section 3.2. The lagged diffusivity iteration associated to the final linearization of the measurement model can be interpreted to produce a Gaussian posterior for the conductivity perturbation, with its mean and covariance given by (3.13) and (3.14), respectively, cf. Remark 3.1. This covariance is finally used as Γ_{prior} in (3.2) and indirectly in (4.1) to enable finding new, more informative positions for the available electrodes via minimizing the induced A-optimality target.

In the following numerical tests, we choose the values $T = 10^{-6}$, $\gamma = 10^5$, $c_v = 300$ and $b_v = 0.01$ for the free parameters in (3.5) and compute reconstructions of the conductivity perturbation by applying five lagged diffusivity steps to each of five subsequent linearizations, which results in reconstructions of the conductivity perturbation that are adequately in line with the smoothed TV prior. We do not consider choosing the number of lagged diffusivity steps or sequential linearizations in more detail here but instead refer to [10, 24, 25, 26] for more information on this aspect in different settings.

Let us first consider the symmetric initial electrode configuration presented on the top row of Figure 5.1. The reconstruction computed from the associated measurements is presented at top in Figure 5.6, with the diagonal of the accompanying posterior covariance visualized in the bottom images of the same figure. Although the diagonal of the posterior covariance, which is used as the prior for finding new positions for the electrodes, does not reveal all characteristics of the associated Gaussian distribution, it in any case indicates that the highest variances in the nodal degrees of freedom in the conductivity reconstruction are found close to the boundaries of the reconstructed inhomogeneity. It is thus to be expected that the minimization of Ψ_A leads to the electrodes moving to positions where more information about the corresponding area of high uncertainty can be obtained.

Indeed, running Algorithm 1 with the prior visualized at bottom in Figure 5.6 results in the electrode positions shown in the top row of Figure 5.7. As expected, most electrodes have gathered close to the edges in the reconstruction formed from the data simulated with the initial electrode setup. Since the electrodes have heavily clustered during the optimization process, it is almost inevitable that the depicted A-optimized positions only correspond to a local minimum of Ψ_A as the electrodes presumably block one another's paths to more optimal positions.

The bottom row of Figure 5.7 presents the electrode setup that results from min-

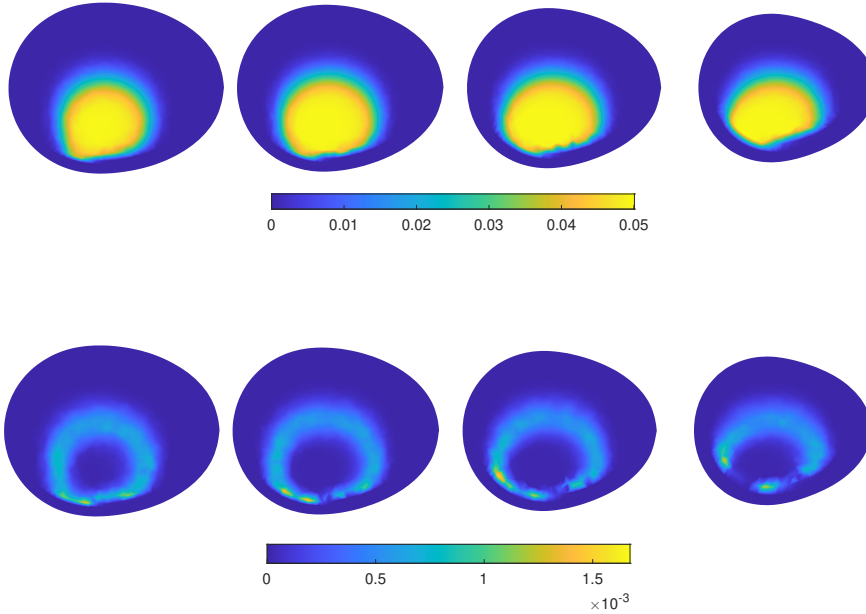


Fig. 5.6: Top: cross-sections of the reconstruction of the conductivity perturbation shown in Figure 5.5 for the symmetric initial electrode configuration in Figure 5.1. Bottom: the diagonal of the corresponding posterior covariance. The horizontal slices are at heights 3 cm, 4 cm, 5 cm and 6 cm.

imizing Ψ_A with the prior covariance obtained as a side product when reconstructing the conductivity perturbation from data simulated with the electrodes concentrated around the right posterior quadrant of the head shown on the bottom row of Figure 5.1. Since the electrodes lie initially closer to the inclusion, the obtained reconstruction of the perturbation (not shown here) is somewhat better localized to the vicinity of the true conductivity perturbation. This leads to the A-optimized electrode positions also being slightly closer to the location of the stroke than on the top row of Figure 5.7, where a couple of electrodes even remain on the uninteresting side of the head.

The evolution of the square root of the A-optimality target, i.e., $\tilde{\Psi}_A$, for the optimization processes leading to the two electrode configurations in Figure 5.7 are plotted in Figure 5.8. Note that the values of $\tilde{\Psi}_A$ in the two convergence plots are not comparable as such because they correspond to two separate priors containing different levels of information on the whereabouts of the conductivity perturbation.

The idea of computing a reconstruction and finding new positions for the available electrodes based on the covariance matrix formed as a side product of the reconstruction algorithm of Section 3.2 can be iterated. Indeed, a reconstruction computed from data simulated with the bottom electrode setup in Figure 5.7 is illustrated at top in Figure 5.9, and the resulting newly A-optimized electrode setup is presented at bottom in that same figure. Since the electrodes shown in the bottom row of Figure 5.7 are positioned closer to the location of the stroke than the symmetric initial electrode configuration in Figure 5.1, the reconstruction in Figure 5.9 is somewhat more accu-

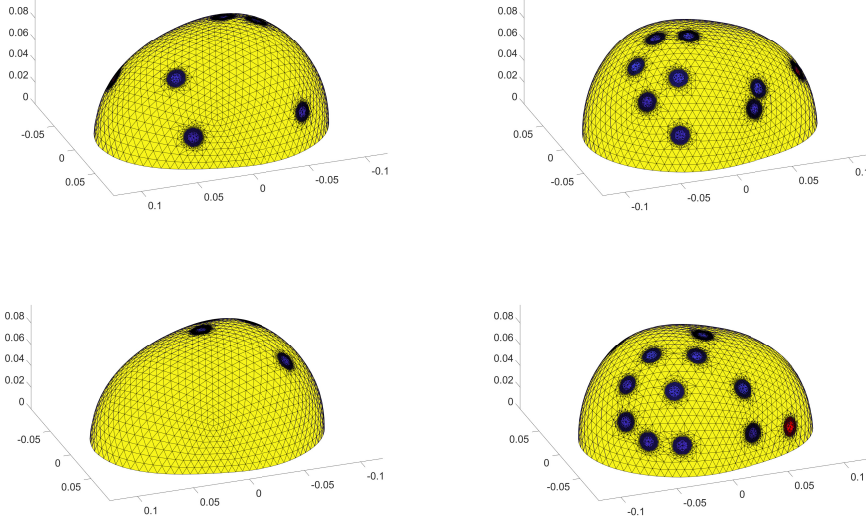


Fig. 5.7: Top: the electrode configuration optimized based on the (prior) covariance obtained as a side product when forming the reconstruction in Figure 5.6 from data corresponding to the symmetric electrode configuration in Figure 5.1. Bottom: the electrode configuration optimized based on the (prior) covariance obtained as a side product when forming a reconstruction from data corresponding to the electrode configuration concentrated around the right posterior quadrant in Figure 5.1.

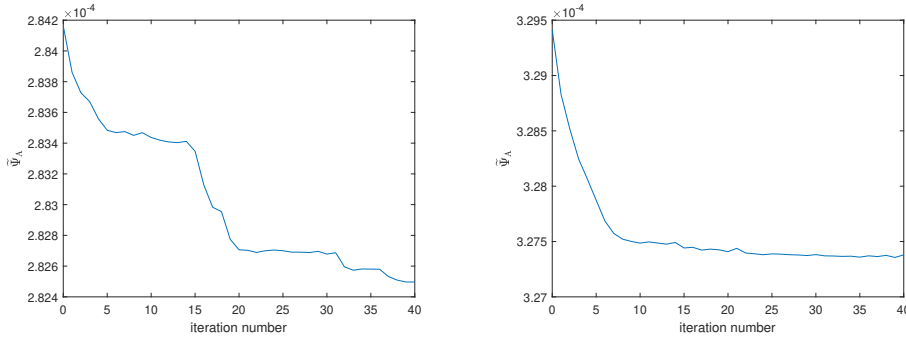


Fig. 5.8: The evolution of $\tilde{\Psi}_A$ during Algorithm 1. Left: the prior covariance is obtained by forming a reconstruction from data simulated with the symmetric electrode configuration in Figure 5.1. Right: the prior covariance is obtained by forming a reconstruction from data simulated with the electrode configuration concentrated around the right posterior quadrant in Figure 5.1.

rate than that in Figure 5.6. This is also reflected in the (doubly) optimized electrodes in Figure 5.9 being more tightly packed around the location of the stroke than either of the (singly) optimized configurations in Figure 5.7.

6. Concluding remarks. This paper tackled the optimization of electrode positions in head imaging by EIT, with the underlying motivation to monitor stroke patients in intensive care. After linearizing the smoothed CEM to introduce an

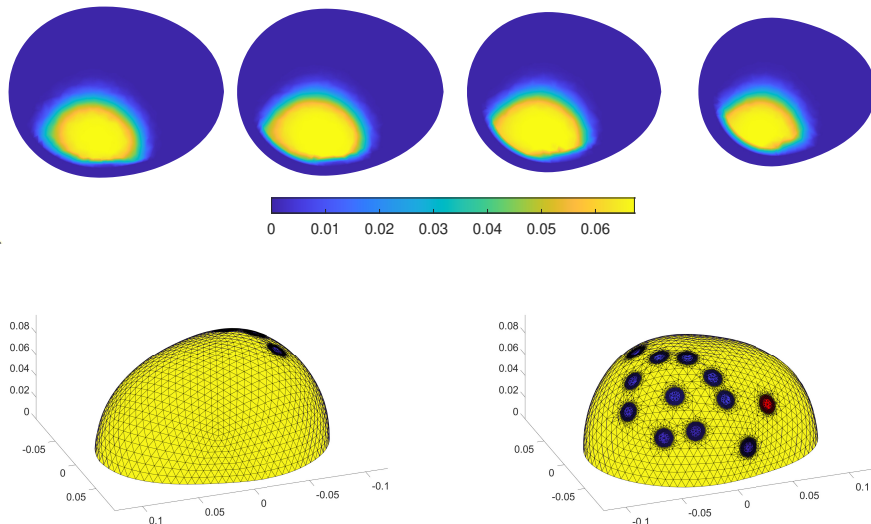


Fig. 5.9: Top: cross-sections of the reconstruction of the conductivity perturbation shown in Figure 5.5 for the electrode configuration at bottom in Figure 5.7. Bottom: the electrode configuration optimized based on the covariance obtained as a side product when forming the presented reconstruction.

approximate linear forward model, two algorithms based on the concept of Bayesian A-optimality were introduced. The first one can be run offline to find informative positions for the available electrodes assuming a Gaussian prior for the conductivity perturbation and assigning a ROI inside the patient’s head. The second algorithm is an extension of the first one, with the Gaussian prior for the optimization process produced by a reconstruction method based on an initial electrode configuration and a combination of sequential linearizations and the lagged diffusivity iteration. Both algorithms produced intuitively acceptable results in the sense that the electrodes moved closer to the area of interest during the optimization process. In particular, the first algorithm led to significant reductions in the expected squared L^2 reconstruction errors under the linearized forward model.

Interesting topics for future research include simultaneous optimization of the electrode positions and employed current patterns (cf. [32, 33]) as well as studying the effect of the particular anatomy of the patient on the optimal electrode positions. In this work, we mainly ignored the choice of the feeding electrode, although it certainly affects optimal configurations and the associated expected reconstruction errors, and we only considered a single head anatomy. Moreover, the introduced gradient-based optimization scheme should in the future be compared with a sparsification approach [3, 4, 27] for choosing the optimal electrode positions.

Acknowledgements. We would like to thank Valentina Candiani for her help with the computational head model.

- [1] ALEXANDERIAN, A. Optimal experimental design for infinite-dimensional Bayesian inverse problems governed by PDEs: A review. *Inverse Problems* (2021), 043001.
- [2] ALEXANDERIAN, A., GLOOR, P. J., GHATTAS, O., ET AL. On Bayesian A- and D-optimal experimental designs in infinite dimensions. *Bayesian Anal.* 11, 3 (2016), 671–695.
- [3] ALEXANDERIAN, A., PETRA, N., STADLER, G., AND GHATTAS, O. A-optimal design of experiments for infinite-dimensional Bayesian linear inverse problems with regularized l_0 -sparsification. *SIAM J. Sci. Comput.* 36, 5 (2014), A2122–A2148.
- [4] ALEXANDERIAN, A., PETRA, N., STADLER, G., AND GHATTAS, O. A fast and scalable method for A-optimal design of experiments for infinite-dimensional Bayesian nonlinear inverse problems. *SIAM J. Sci. Comput.* 38, 1 (2016), A243–A272.
- [5] BARDSLEY, J. M. *Computational uncertainty quantification for inverse problems*, vol. 19 of *Computational Science & Engineering*. Society for Industrial and Applied Mathematics (SIAM), Philadelphia, PA, 2018.
- [6] BORCEA, L. Electrical impedance tomography. *Inverse problems* 18 (2002), R99–R136.
- [7] BURGER, M., HAUPTMANN, A., HELIN, T., HYVÖNEN, N., AND PUSKA, J.-P. Sequentially optimized projections in x-ray imaging. *Inverse Problems* 37 (2014), 0750006.
- [8] CALVETTI, D., AND SOMERSALO, E. Hypermodels in the Bayesian imaging framework. *Inverse Problems* 24 (2008), 034013.
- [9] CANDIANI, V., HANNUKAINEN, A., AND HYVÖNEN, N. Computational framework for applying electrical impedance tomography to head imaging. *SIAM J. Sci. Comput.* 41 (2019), B1034–B1060.
- [10] CANDIANI, V., HYVÖNEN, N., KAIPIO, J. P., AND KOLEHMAINEN, V. Approximation error method for imaging the human head by electrical impedance tomography. *Inverse Problems* 37, 12 (2021), 125008.
- [11] CANDIANI, V., AND SANTACESARIA, M. Neural networks for classification of stroke in electrical impedance tomography on a 3D head model. *Mathematics in Engineering* 4 (2022), 1–22.
- [12] CHALONER, K., AND VERDINELLI, I. Bayesian experimental design: A review. *Stat. Sci.* (1995), 273–304.
- [13] CHAN, T. F., AND MULET, P. On the convergence of the lagged diffusivity fixed point method in total variation image restoration. *SIAM J. Numer. Anal.* 36, 2 (1999), 354–367.
- [14] CHENEY, M., ISAACSON, D., AND NEWELL, J. Electrical impedance tomography. *SIAM Rev.* 41 (1999), 85–101.
- [15] CHENG, K.-S., ISAACSON, D., NEWELL, J. S., AND GISSER, D. G. Electrode models for electric current computed tomography. *IEEE Trans. Biomed. Eng.* 36 (1989), 918–924.
- [16] COLTON, D., AND KRESS, R. *Inverse acoustic and electromagnetic scattering theory*, second ed., vol. 93 of *Applied Mathematical Sciences*. Springer-Verlag, Berlin, 1998.
- [17] DARDÉ, J., HAKULA, H., HYVÖNEN, N., AND STABOULIS, S. Fine-tuning electrode information in electrical impedance tomography. *Inverse Probl. Imag.* 6 (2012), 399–421.
- [18] DARDÉ, J., HYVÖNEN, N., KUUTELA, T., AND VALKONEN, T. Contact adapting electrode model for electrical impedance tomography. *SIAM J. Appl. Math.* 82 (2022), 427–229.
- [19] DOBSON, D. C., AND VOGEL, C. R. Convergence of an iterative method for total variation denoising. *SIAM J. Numer. Anal.* 34, 5 (1997), 1779–1791.
- [20] DUONG, D.-L., HELIN, T., AND ROJO-GARCIA, J. R. Stability estimates for the expected utility in Bayesian optimal experimental design. *Inverse Problems* 39 (2022), 125008.
- [21] GABRIEL, S., LAU, R. W., AND GABRIEL, C. The dielectric properties of biological tissues: II. Measurements in the frequency range 10 Hz to 20 GHz. *Phys. Med. Biol.* 41 (1996), 2251.
- [22] HANKE, M., HARRACH, B., AND HYVÖNEN, N. Justification of point electrode models in electrical impedance tomography. *Math. Models Methods Appl. Sci.* 21 (2011), 1395–1413.
- [23] HANNUKAINEN, A., HYVÖNEN, N., AND PERKKIÖ, L. Inverse heat source problem and experimental design for determining iron loss distribution. *SIAM J. Sci. Comput.* 43 (2021), B243–B270.
- [24] HARHANEN, L., HYVÖNEN, N., MAJANDER, H., AND STABOULIS, S. Edge-enhancing reconstruction algorithm for three-dimensional electrical impedance tomography. *SIAM J. Sci. Comput.* 37 (2015), B60–B78.
- [25] HELIN, T., HYVÖNEN, N., J., M., AND PUSKA, J.-P. Bayesian design of measurements for magnetorelaxometry imaging. *Inverse Problems* (2023), 125020.
- [26] HELIN, T., HYVÖNEN, N., AND PUSKA, J.-P. Edge-promoting adaptive Bayesian experimental design for x-ray imaging. *SIAM J. Sci. Comput.* 44 (2022), B506–B530.
- [27] HORESH, L., HABER, E., AND TENORIO, L. Optimal Experimental Design for the Large-Scale Nonlinear Ill-Posed Problem of Impedance Imaging, in *‘Large-Scale Inverse Problems and Quantification of Uncertainty’*. Wiley, 2010.
- [28] HYVÖNEN, N., AND MUSTONEN, L. Smoothened complete electrode model. *SIAM J. Appl.*

- Math.* 77 (2017), 2250–2271.
- [29] HYVÖNEN, N., AND MUSTONEN, L. Generalized linearization techniques in electrical impedance tomography. *Numer. Math.* 140 (2018), 95–120.
- [30] HYVÖNEN, N., SEPPÄNEN, A., AND STABOULIS, S. Optimizing electrode positions in electrical impedance tomography. *SIAM J. Appl. Math.* 74 (2014), 1831–1851.
- [31] KAIPIO, J., AND SOMERSALO, E. *Statistical and Computational Inverse Problems*, vol. 160. Springer Science & Business Media, 2006.
- [32] KAIPIO, J. P., SEPPÄNEN, A., SOMERSALO, E., AND HAARIO, H. Posterior covariance related optimal current patterns in electrical impedance tomography. *Inverse Problems* 20 (2004), 919–936.
- [33] KAIPIO, J. P., SEPPÄNEN, A., VOUTILAINEN, A., AND HAARIO, H. Optimal current patterns in dynamical electrical impedance tomography imaging. *Inverse Problems* 23 (2007), 1201–1214.
- [34] KARIMI, A., TAGHIZADEH, L., AND HEITZINGER, C. Optimal Bayesian experimental design for electrical impedance tomography in medical imaging. *Comput. Methods Appl. Mech. Eng.* 373 (2021), 113489.
- [35] LAI, Y., VAN DRONGELEN, W., DING, L., HECOX, K. E., TOWLE, V. L., FRIM, D. M., AND HE, B. Estimation of in vivo human brain-to-skull conductivity ratio from simultaneous extra-and intra-cranial electrical potential recordings. *Clin. Neurophysiol.* 116 (2005), 456–465.
- [36] LASSAS, M., AND SILTANEN, S. Can one use total variation prior for edge-preserving bayesian inversion? *Inverse Problems* 20, 5 (2004), 1537.
- [37] LATIKKA, J. A., HYTINEN, J. A., KUURNE, T. A., ESKOLA, H. J., AND MALMIVUO, J. A. The conductivity of brain tissue: Comparison of results in vivo and in vitro measurement. In *Proceedings of the 23rd Annual International Conference of the IEEE Engineering in Medicine and Biology Society* (Instanbul, Turkey, October 2001), vol. 4, IEEE, pp. 910–912.
- [38] LEE, E., DUFFY, W., HADIMANI, R., WARIS, M., SIDDIQUI, W., ISLAM, F., RAJAMANI, M., NATHAN, R., AND JILES, D. Investigational effect of brain-scalp distance on the efficacy of transcranial magnetic stimulation treatment in depression. *IEEE Trans. Magn.* 52 (2016), 1–4.
- [39] MCCANN, H., PISANO, G., AND BELTRACHINI, L. Variation in reported human head tissue electrical conductivity values. *Brain Topogr.* 32 (2019), 825–858.
- [40] NOCEDAL, J., AND WRIGHT, S. J. *Numerical optimization*, second ed. Springer, New York, 2006.
- [41] OOSTENDORP, T. F., DELBEKE, J., AND STEGEMAN, D. F. The conductivity of the human skull: results of in vivo and in vitro measurements. *IEEE Trans. Biomed. Eng.* 47 (2000), 1487–1492.
- [42] RAINFORTH, T., FOSTER, A., IVANOVA, D. R., AND SMITH, F. B. Modern Bayesian experimental design. *arXiv preprint arXiv:2302.14545* (2023).
- [43] RUDIN, L. I., OSHER, S., AND FATEMI, E. Nonlinear total variation based noise removal algorithms. *Physica D* 60 (1992), 259–268.
- [44] RYAN, E. G., DROVANDI, C. C., MCGREE, J. M., AND PETTITT, A. N. A review of modern computational algorithms for Bayesian optimal design. *Int. Stat. Rev.* 84, 1 (2016), 128–154.
- [45] SMYL, D., AND LIU, D. Optimizing electrode positions in 2-D electrical impedance tomography using deep learning. *IEEE Trans. Instrum. Meas.* 69, 9 (2020), 6030–6044.
- [46] SOMERSALO, E., CHENEY, M., AND ISAACSON, D. Existence and uniqueness for electrode models for electric current computed tomography. *SIAM J. Appl. Math.* 52 (1992), 1023–1040.
- [47] TOIVANEN, J., HÄNNINEN, A., SAVOLAINEN, T., FORSS, N., AND KOLEHMAINEN, V. 8 - monitoring hemorrhagic strokes using eit. In *Bioimpedance and Spectroscopy*, P. Annus and M. Min, Eds. Academic Press, 2021, pp. 271–298.
- [48] UHLMANN, G. Electrical impedance tomography and Calderón’s problem. *Inverse Problems* 25 (2009), 123011.
- [49] VAUHKONEN, M. *Electrical impedance tomography with prior information*, vol. 62. Kuopio University Publications C (Dissertation), 1997.
- [50] VAUHKONEN, P. J., VAUHKONEN, M., SAVOLAINEN, T., AND KAIPIO, J. P. Three-dimensional electrical impedance tomography based on the complete electrode model. *IEEE Trans. Biomed. Eng.* 46 (1999), 1150–1160.
- [51] VOGEL, C. R., AND OMAN, M. E. Iterative methods for total variation denoising. *SIAM J. Sci. Comput.* 17 (1996), 227–238.